

RESEARCH

Open Access



# Ultrasound-responsive nanoparticles for nitric oxide release to inhibit the growth of breast cancer

Haiyan Yang<sup>1,6†</sup>, Guangrong Zheng<sup>2,6†</sup>, GuoChen Li<sup>2,6†</sup>, Jincui Chen<sup>1</sup>, Licui Qi<sup>1</sup>, Yong Luo<sup>3,6</sup>, Tengfei Ke<sup>4\*</sup>, Jie Xiong<sup>5\*</sup> and Xiaojuan Ji<sup>1,7\*</sup>

## Abstract

Gas therapy represents a promising strategy for cancer treatment, with nitric oxide (NO) therapy showing particular potential in tumor therapy. However, ensuring sufficient production of NO remains a significant challenge. Leveraging ultrasound-responsive nanoparticles to promote the release of NO is an emerging way to solve this challenge. In this study, we successfully constructed ultrasound-responsive nanoparticles, which consisted of poly (D, L-lactide-co-glycolic acid) (PLGA) nanoparticles, natural L-arginine (LA), and superparamagnetic iron oxide nanoparticles (SPIO, Fe<sub>3</sub>O<sub>4</sub> NPs), denote as Fe<sub>3</sub>O<sub>4</sub>-LA-PLGA NPs. The Fe<sub>3</sub>O<sub>4</sub>-LA-PLGA NPs exhibited effective therapeutic effects both in vitro and in vivo, particularly in NO-assisted antitumor gas therapy and photoacoustic (PA) imaging properties. Upon exposure to ultrasound irradiation, LA and Fe<sub>3</sub>O<sub>4</sub> NPs were rapidly released from the PLGA NPs. It was demonstrated that LA could spontaneously react with hydrogen peroxide (H<sub>2</sub>O<sub>2</sub>) present in the tumor microenvironment to generate NO for gas therapy. Concurrently, Fe<sub>3</sub>O<sub>4</sub> NPs could rapidly react with H<sub>2</sub>O<sub>2</sub> to produce a substantial quantity of reactive oxygen species (ROS), which can oxidize LA to further facilitate the release of NO. In conclusion, the proposed ultrasound-responsive NO delivery platform exhibits significant potential in effectively inhibiting the growth of breast cancer.

**Keywords** Breast cancer, Ultrasound, Nitric oxide, Gas therapy

<sup>†</sup>Haiyan Yang, Guangrong Zheng and GuoChen Li contributed equally to this work.

\*Correspondence:

Tengfei Ke

ketengfei@kmmu.edu.cn

Jie Xiong

xj306654@hospital.cqmu.cn

Xiaojuan Ji

400146@cqmu.edu.cn

<sup>1</sup>Department of Ultrasound, Chongqing General Hospital, Chongqing University, Chongqing 401147, China

<sup>2</sup>Department of Radiology, Yan'an Hospital, Affiliated to Kunming Medical University, Yan'an Hospital of Kunming City, Kunming 650051, China

<sup>3</sup>Department of Ultrasound, The People's Hospital of Chongqing Liang Jiang New Area, Chongqing 400010, China

<sup>4</sup>Department of Radiology, Yunnan Cancer Hospital (The Third Affiliated Hospital of Kunming Medical University, Peking University Cancer Hospital Yunnan Campus), Kunming 650118, China

<sup>5</sup>Institute of Ultrasound Imaging, The Second Affiliated Hospital of Chongqing Medical University, Chongqing 400010, China

<sup>6</sup>State Key Laboratory of Ultrasound in Medicine and Engineering, College of Biomedical Engineering, Chongqing Medical University, Chongqing 400016, China

<sup>7</sup>Department of Ultrasound, National Clinical Research Center for Child Health and Disorders, Ministry of Education Key Laboratory of Child Development and Disorders, Chongqing Key Laboratory of Child Rare Diseases in Infection and Immunity, Children's Hospital of Chongqing Medical University, Chongqing 400016, China



## Introduction

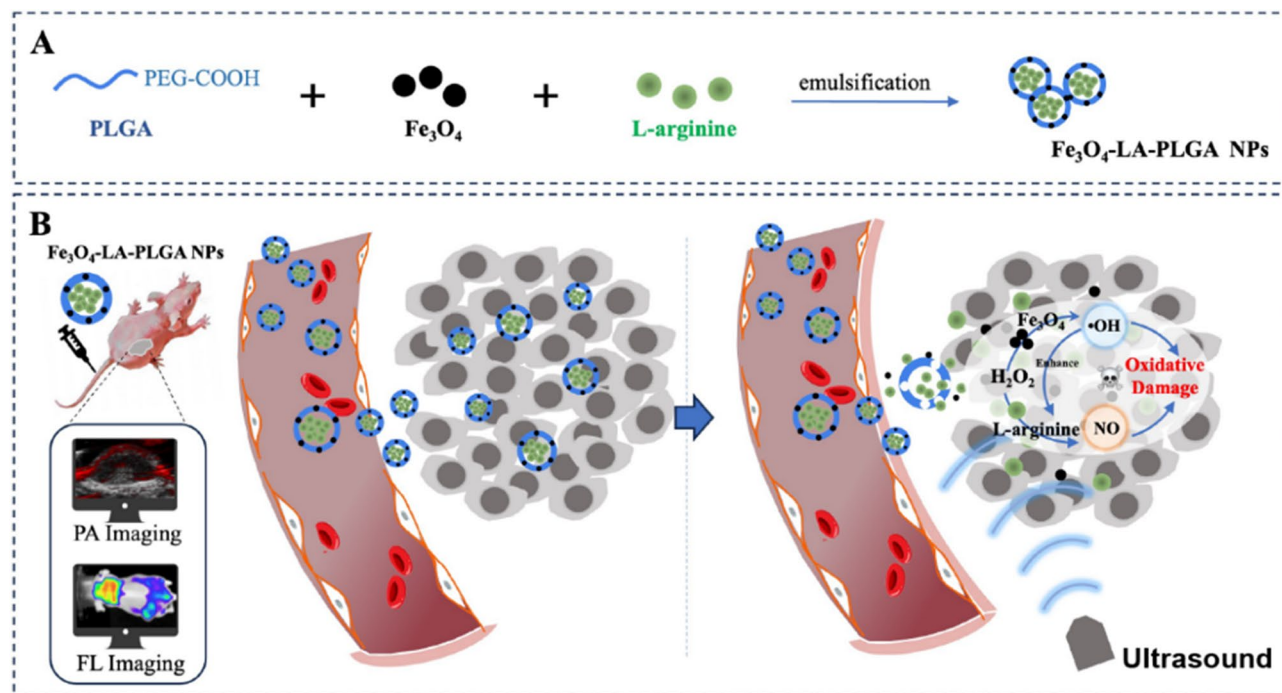
Breast cancer represents the primary cause of cancer-related mortality among women worldwide [1–3]. While traditional treatment modalities, such as surgery, chemotherapy, and radiotherapy, can be efficacious in certain cases, they do not constitute a comprehensive solution [4–6]. The overall survival rate for patients with breast cancer remains low due to the aggressive nature of the disease and its poor prognosis [7–9]. Therefore, it is imperative to develop new therapeutic strategies for patients with breast cancer. In recent years, gas therapy has emerged as a promising therapeutic modality for tumors, attracting significant attention due to its high efficacy and favorable biological safety profile [10–12]. It has been extensively investigated in numerous anti-tumor applications, including gas-induced tumor cell killing, enhanced radiation therapy (RT) sensitization [13, 14], chemotherapy [15–17], photothermal therapy (PTT) [18, 19], photodynamic therapy (PDT) [20], and sonodynamic therapy (SDT) [21]. Nitric oxide (NO) is a prominent therapeutic gas in cancer therapy. It has been demonstrated to inhibit the growth of tumor cells through various mechanisms, including mitochondrial inhibition, DNA damage, nitrosylation of enzymes, and inhibition of cellular respiration. These effects have been observed at high concentrations ( $>1\mu\text{M}$ ), resulting in an excellent anti-tumor effect [22–24]. However, it is unfortunate that low NO concentrations can even promote tumor cell growth [25, 26]. Thus, enhancing NO concentration is a crucial aspect of effective NO gas therapy.

The direct utilization of free NO gas is limited by its short half-life and vulnerability to diverse biological substances (e.g., glutathione (GSH), hemoglobin, superoxide, and molecular oxygen) [24]. Therefore, numerous versatile nanoplatfroms loaded with NO donors or NO-releasing molecules have been explored to deliver NO in a straightforward and precise manner. A plethora of NO-releasing donors e.g., N, N'-di-sec-Butyl-N, N'-dinitroso-1,4-phenylenediamine (BNN6), S-nitrosothiols (SNO), S-nitroso glutathione (GSNO), and Rusen black salt (RBS)) have been explored to release NO under the external stimuli, including light (UV-vis/near-infrared laser), X-ray, and ultrasound [27–32]. However, previous NO-releasing donors have been found to be unsafe for biological applications due to their toxic production. Therefore, it is urgent to develop a biosafe and efficient strategy to achieve high capacity and controllable NO release.

L-Arginine (LA) is a naturally occurring NO-releasing donor with high biocompatibility and the capacity to produce NO in the presence of inducible NO synthase [10, 33]. Furthermore, LA can spontaneously release NO when reacting with hydrogen peroxide ( $\text{H}_2\text{O}_2$ ) [34],

which is commonly abundant in tumor cells compared to normal cells [35]. In normal conditions, the release amount and speed of LA and  $\text{H}_2\text{O}_2$  is relatively slow. Our previous study demonstrated that the release of NO can be rapid and in large quantities over a short period of time when the presence of superparamagnetic iron oxide nanoparticles (SPIO,  $\text{Fe}_3\text{O}_4$  NPs) act as a catalyst [36]. It is well established that  $\text{H}_2\text{O}_2$  can react with  $\text{Fe}^{2+}$  to produce reactive oxygen species (ROS) containing hydroxyl radicals ( $\cdot\text{OH}$ ) and hydroxide ions ( $\text{OH}^-$ ), which is known as the Fenton reaction [37, 38]. The greater the quantity of ROS generated, the more effectively it can oxidize LA to generate more NO [39].  $\text{Fe}_3\text{O}_4$  NPs have been widely used for *in vivo* biomedical applications, Moreover, functioning as an “optical absorber”,  $\text{Fe}_3\text{O}_4$  NPs can generate noninvasive photoacoustic (PA) imaging contrast agent enhancement when stimulated by laser irradiation at specific wavelengths [40].

Herein, in this study, we successfully constructed ultrasound-responsive nanoparticles for the rapid and controlled release of NO, which has been shown to inhibit breast cancer by utilizing NO as the antitumor therapeutic gas. Poly-lactide-co-glycolide (PLGA) is a nanosized polymeric material with high biodegradability and biocompatibility that has been approved by the Food and Drug Administration (FDA) for medical applications. We rationally designed and synthesized a versatile PLGA nanoparticle, encapsulating the natural LA as a NO donor in the core and  $\text{Fe}_3\text{O}_4$  NPs packed in the shell as a stable nanoparticle to respond to ultrasound-responsive therapeutic agent (denoted as  $\text{Fe}_3\text{O}_4$ -LA-PLGA NPs). The  $\text{Fe}_3\text{O}_4$ -LA-PLGA NPs demonstrated efficacious therapeutic effects through NO-assisted antitumor gas therapy. As illustrated in Scheme 1,  $\text{Fe}_3\text{O}_4$ -LA-PLGA NPs can accumulate into the tumor region via the enhanced permeability and retention (EPR) effect after intravenous injection. The distribution of  $\text{Fe}_3\text{O}_4$ -LA-PLGA NPs can be monitored via photoacoustic (PA) imaging. Upon exposure to ultrasound irradiation, LA and  $\text{Fe}_3\text{O}_4$  NPs were released rapidly from the PLGA NPs due to the interaction of mechanical effects of ultrasound, thereby initiating a cascade of reactions. LA can spontaneously react with  $\text{H}_2\text{O}_2$  present in the tumor microenvironment to generate NO for gas therapy. Simultaneously, the integrated  $\text{Fe}_3\text{O}_4$  NPs can rapidly react with  $\text{H}_2\text{O}_2$  to produce a substantial quantity of reactive oxygen species (ROS). Moreover, the generated ROS can oxidize LA to facilitate the release of NO. Ultimately, a synergistic cascade amplification reaction is achieved. The results of this study suggest that ultrasound-responsive nanoparticles have significant potential as a delivery platform for NO, with the potential to inhibit cancer growth.



**Scheme 1** Design of ultrasound-responsive nanoparticles for nitric oxide release to inhibit breast cancer growth

## Materials and methods

PLGA-PEG-COOH (50: 50, MW: 15 000) was purchased from Daigang BIO Engineer Ltd, Co. (Shan Dong, China). Poly (vinyl alcohol) (PVA) was purchased from Sigma-Aldrich Chemical Co., Ltd., (St. Louis, MO, USA). Trichloromethane (CHCl<sub>3</sub>) was purchased from Chongqing East Chemical Industry Ltd, Co. (China). L-Arginine was purchased from Sigma-Aldrich (USA), and iron oxide nanoparticles (10 nm, 25 mg mL<sup>-1</sup>) were purchased from Ocean Nanotech Co. Ltd (USA). The cell counting kit (CCK-8) and calcein & propidium iodide (PI) apoptosis assay kit were purchased from Dojindo Laboratories (Kumamoto, Japan). 3-Amino,4-aminomethyl-2',7'-difluorescein, diacetate (DAF-FM DA), 2,7-Dichlorodihydrofluorescein diacetate (DCFH-DA), a nitric oxide assay kit (Griess assay kit), 4,6-diamidino-2-phenylindole (DAPI), and 1,1'-dioctadecyl-3,3,3',3'-tetramethylindotricarbocyanine iodide (DiR) were purchased from Beyotime Biotechnology Co., Ltd (China).

### Preparation of Fe<sub>3</sub>O<sub>4</sub>-LA-PLGA NPs

The Fe<sub>3</sub>O<sub>4</sub>-LA-PLGA NPs were prepared via the ultrasound double emulsion (water/oil/water, W/O/W) method. First, 150 mg PLGA-PEG-COOH (50: 50, MW: 15 000) and 10 mg Fe<sub>3</sub>O<sub>4</sub> NPs were completely dissolved in 2 mL of CHCl<sub>3</sub>. Then, 0.4 mL solution of LA (100 mg/mL in pure water) was added, and the mixture was sonicated with an ultrasonic cell crusher at 105 W for 2 min to obtain the W/O emulsion; subsequently, 4 mL of PVA solutions (w/v=4%) was added, and the mixture

was emulsified again at 105 W for 5 min to obtain the W/O/W emulsion. Next, 8 mL of isopropyl alcohol solution (w/v=2%) was added, and the mixture was stirred to volatilize the CHCl<sub>3</sub>. Finally, the Fe<sub>3</sub>O<sub>4</sub>-LA-PLGA NPs were collected following centrifugation (10 000 rpm, 10 min) and stored at 4 °C for subsequent utilization. The fluorescent Fe<sub>3</sub>O<sub>4</sub>-LA-PLGA NPs were prepared by a similar procedure, with DiR added to the mixture.

### Characterization of Fe<sub>3</sub>O<sub>4</sub>-LA-PLGA NPs

Transmission electron microscopy (TEM, Hitachi 7500, Tokyo, Japan) was employed to observe the structure of Fe<sub>3</sub>O<sub>4</sub>-LA-PLGA NPs. The Nano ZS90 Zetasizer (Malvern Panalytical, Ltd., Malvern, UK) was employed to ascertain the size distribution and Zeta potential of Fe<sub>3</sub>O<sub>4</sub>-LA-PLGA NPs. Fluorescence (FL) images were acquired using the LB983 imaging system (Berthold Technologies GmbH & Co. KG, Germany). Photoacoustic (PA) images were obtained using the Vevo LAZR PA Imaging System (Visual Sonics Inc., Toronto, Canada). Confocal laser scanning microscope (CLSM) images were captured using a Nikon optical microscope (Japan). The flow cytometry assay was employed by Beckman Coulter (American).

### LA loading content, Encapsulation Efficiency, LA and NO release determination

The ultraviolet-visible spectrophotometer (UV-vis) (Shimadzu UV 2600, Kyoto, Japan) was employed to generate the standard curve for LA, and the drug loading capacity

(DL) and encapsulation efficiency (EE) of LA were quantified and evaluated in accordance with the following equations:

$$DL(\%) = \frac{\text{amount of total LA applied (mg)} - \text{amount of LA in the supernatant (mg)}}{\text{amount of dried nanoparticle (mg)}} \times 100\%$$

$$EE(\%) = \frac{\text{amount of total LA applied (mg)} - \text{amount of LA in the supernatant (mg)}}{\text{amount of total LA applied (mg)}} \times 100\%$$

The ultrasound-triggered release of LA was performed in an aqueous system. Briefly, Fe<sub>3</sub>O<sub>4</sub>-LA-PLGA NPs (containing 10 mg PLGA, respectively) were dispersed in 4 mL of PBS. Then, the mixture was irradiated with or without ultrasound (Chongqing Haifu Technology, China) at a frequency of 200 kHz and a power density of 2 W for a duration of 200 S. The release profile of LA was analyzed by UV-vis spectrometer post purification with centrifugation (10000 rpm, 10 min) at different intervals (1 min, 2 min, 3 min, 5 min, 10 min, 20 min, and 30 min) after ultrasound irradiation. The NO release was quantified using the Griess assay kit. In brief, Fe<sub>3</sub>O<sub>4</sub>-LA-PLGA NPs, Fe<sub>3</sub>O<sub>4</sub>-PLGA NPs, and LA-PLGA NPs (containing 10 mg PLGA, respectively) were dispersed in 1 mL PBS and mixed with an excess of H<sub>2</sub>O<sub>2</sub> (50 μM). Subsequently, the mixture was irradiated with or without ultrasound. The NO release was quantified by means of a Griess assay kit at various time points (1 min, 2 min, 3 min, 5 min, 10 min, 20 min, and 30 min) following ultrasound irradiation.

#### Cell culture and MDA-MB-231 tumor-bearing mouse model

The human breast cancer MDA-MB-231 cells and Human umbilical vein endothelial cells (HUVECs) were obtained from the Chinese Academy of Sciences Cell Bank (China). The cells were cultured at 37 °C with 5% CO<sub>2</sub> in DMEM, which was supplemented with 10% FBS and 1% streptomycin/penicillin. A total of 0.1 mL of PBS solution (containing 1×10<sup>6</sup> MDA-MB-231 cells) was injected subcutaneously into the left flank of female BALB/c nude mice (weighing between 18 and 20 g) to establish the tumor model. The tumor volume was calculated according to the formula [0.5 × length × (width)<sup>2</sup>]. The biosafety of Fe<sub>3</sub>O<sub>4</sub>-LA-PLGA NPs was evaluated in BALB/c mice. All animal care and use procedures were reviewed and approved by the Animal Ethics Committee of Chongqing Medical University.

#### In vitro cytotoxicity assay

To assess the cytotoxicity and growth inhibition of Fe<sub>3</sub>O<sub>4</sub>-LA-PLGA NPs in vitro, we conducted a series of co-incubation experiments involving different concentrations of NPs (0.1, 0.25, 0.5, 1.0, 2.5, 5.0, and 10 mg/mL) and MDA-MB-231 cells (or HUVECs) at 37 °C, with or without ultrasound irradiation. The cell viability was assessed by the cell counting kit-8 (CCK-8) assay (*n*=5).

Furthermore, the viable and dead cells were co-stained with calcein-AM and propidium iodide (PI), and their distribution was observed by CLSM.

#### Ultrasound-responsive intracellular ROS and NO release

To assess the impact of ultrasound irradiation on intracellular ROS and NO release, MDA-MB-231 cells (1×10<sup>5</sup>) were randomly allocated to eight experimental groups: control, Fe<sub>3</sub>O<sub>4</sub>-PLGA NPs, LA-PLGA NPs, Fe<sub>3</sub>O<sub>4</sub>-LA-PLGA NPs, ultrasound irradiation (US), Fe<sub>3</sub>O<sub>4</sub>-PLGA NPs+US, LA-PLGA NPs+US, and Fe<sub>3</sub>O<sub>4</sub>-LA-PLGA NPs+US. Cells in the first and fifth groups were treated with phosphate buffered saline (PBS), respectively. The remaining groups were treated with Fe<sub>3</sub>O<sub>4</sub>-PLGA NPs, LA-PLGA NPs, and Fe<sub>3</sub>O<sub>4</sub>-LA-PLGA NPs (containing 5 mg PLGA), respectively. After a co-incubation period of 4 h, the cells in the sixth to eighth groups were exposed to ultrasound irradiation. The DCFH-DA and DAF-FM DA NO assay kit was then added and incubated for a further 30 min. The NO release was then qualitatively determined by CLSM.

#### The dual-modality imaging of Fe<sub>3</sub>O<sub>4</sub>-LA-PLGA NPs

For fluorescence (FL) imaging, DiR (Ex/Em:748 nm/780 nm)-labeled Fe<sub>3</sub>O<sub>4</sub>-LA-PLGA NPs (containing 5 mg PLGA) were intravenously injected into MDA-MB-231 tumor-bearing nude mice, FL images were acquired at pre-injection, 1 h, 6 h, 24 h, and 48 h post-injection using the LB983 imaging system. Tumors and major organs were extracted for FL imaging and the corresponding FL intensity was measured.

For PA imaging, Fe<sub>3</sub>O<sub>4</sub>-LA-PLGA NPs (containing 5 mg PLGA) were administered intravenously to MDA-MB-231 tumor-bearing mice. The following assessments were conducted under 690 nm irradiation. PA images were obtained at pre-injection, 1 h, 6 h, 24 h, and 48 h post-injection.

#### Biosafety of Fe<sub>3</sub>O<sub>4</sub>-LA-PLGA NPs

Female BALB/c mice (18–20 g) were randomly divided into five groups (*n*=5 per group), including the control group, the 1-day group, the 3-day group, the 7-day group, and the 14-day group. The control group was intravenously injected with 0.2 mL PBS, and the other groups were intravenously injected with 0.2 mL Fe<sub>3</sub>O<sub>4</sub>-LA-PLGA NPs, respectively. Blood samples were collected one day after injection (control group) and at 1, 3, 7, and 14 days post-injection (Fe<sub>3</sub>O<sub>4</sub>-LA-PLGA NPs) for biochemical examinations. The major organs (heart, liver, spleen, lungs, and kidneys) were stained with hematoxylin-eosin staining (H&E) for histological analysis at the corresponding time point.

### Therapeutic efficacy of Fe<sub>3</sub>O<sub>4</sub>-LA-PLGA NPs

To assess the therapeutic efficacy of Fe<sub>3</sub>O<sub>4</sub>-LA-PLGA NPs, the MDA-MB-231 tumor-bearing nude mice were randomly divided into four groups (five mice per group). The first and second groups of mice were intravenously injected with PBS, setting as the control group and the “US” group, respectively. The second group was also treated with ultrasound irradiation. The third and fourth groups of mice were injected with Fe<sub>3</sub>O<sub>4</sub>-LA-PLGA NPs (containing 5 mg PLGA), which was set as the “NPs” group and the “NPs+US” group, respectively. The fourth group was also treated with ultrasound irradiation. For the two groups subjected to ultrasound irradiation, the tumor sites were irradiated with ultrasound at a frequency of 200 kHz and a power density of 2 W for a duration of 200 s at 24 h post-injection. Tumor volumes and body weights were measured from day 0 to day 11 after the corresponding treatments. On the 11th day following the administration of the respective treatments, the mice were euthanized, and the tumor tissues were harvested for histological analysis. This involved the use of H&E and terminal deoxynucleotidyl transferase-mediated dUTP nick end labeling (TUNEL) to observe apoptosis.

### Statistical analysis

All data are expressed as mean ± standard deviation. The statistical analysis was conducted using the SPSS 21.0 program. Paired *t*-tests and one-way analysis of variance were employed to analyze the data (*p* < 0.05 was considered statistically significant).

## Results and discussion

### Characterization of Fe<sub>3</sub>O<sub>4</sub>-LA-PLGA NPs

The synthesis of Fe<sub>3</sub>O<sub>4</sub>-LA-PLGA NPs is illustrated in Scheme 1A, which depicts the formation of an ultrasonic double emulsion. This method is well established for the encapsulation of both hydrophobic and hydrophilic drugs and bioactive compounds [41]. The transmission electron microscopy (TEM) image indicates that the Fe<sub>3</sub>O<sub>4</sub> NPs were successfully incorporated into the spherical shell, exhibiting a high degree of contrast (Fig. 1A). The obtained Fe<sub>3</sub>O<sub>4</sub>-LA-PLGA NPs exhibited a highly uniform size, with a diameter of 302.4 ± 4.3 nm, which is slightly larger than that of Fe<sub>3</sub>O<sub>4</sub>-PLGA NPs (298.6 ± 3.1 nm), LA-PLGA NPs (295.3 ± 2.7 nm), and PLGA NPs (293.9 ± 2.6 nm) (Fig. 1B). The zeta potential of the NPs was found to be -22.9 ± 2.3 mV, -20.7 ± 3.7 mV, -21.1 ± 4.3 mV, and -31.7 ± 2.4 mV, respectively (Fig. 1C). Moreover, the Fe<sub>3</sub>O<sub>4</sub>-LA-PLGA NPs exhibited excellent stability in a relatively uniform size (Fig. 1D) and zeta potentials (Fig. 1E) over 7 days. Subsequently, the drug loading efficiencies (DL%) and encapsulation (DE%) of LA were quantified by UV spectroscopy, in accordance with the standard curve of LA at 210 nm (Fig. 1F and Fig.

S1). The drugs DL% and EE% were determined to be high at 24.5 ± 2.9 wt % and 81.6 ± 1.3% (Fig. S2), respectively. The high loading capacity of drugs suggests that the FDA-approved PLGA polymers have significant potential as a promising nanocarrier for drug delivery. Moreover, the encapsulation efficiency of Fe<sub>3</sub>O<sub>4</sub> NPs in the Fe<sub>3</sub>O<sub>4</sub>-LA-PLGA NPs was calculated to be 85.0 wt%, indicating that PLGA-based NPs possess high encapsulation efficiency. To assess the cumulative LA release from Fe<sub>3</sub>O<sub>4</sub>-LA-PLGA NPs in PBS with and without ultrasound irradiation. As shown in Fig. S3, Fe<sub>3</sub>O<sub>4</sub>-LA-PLGA NPs exhibited a sustained release of encapsulated LA within 5 min of irradiation, and the accumulative amount of LA reached 70%. We further assessed the NO release by various PLGA NPs in the presence of H<sub>2</sub>O<sub>2</sub> (50 μM) with and without ultrasound irradiation, a standard curve of NO was constructed via the Griess assay (Fig. 1G). The results demonstrated that Fe<sub>3</sub>O<sub>4</sub>-LA-PLGA NPs and LA-PLGA NPs exhibited enhanced NO release in response to ultrasound irradiation. The NO release from Fe<sub>3</sub>O<sub>4</sub>-LA-PLGA NPs was significantly accelerated compared to LA-PLGA NPs in the presence of H<sub>2</sub>O<sub>2</sub> (50 μM) under ultrasound irradiation (Fig. 1H), suggesting that ultrasound could accelerate the burst of the PLGA-based NPs, especially the catalytic effect of Fe<sub>3</sub>O<sub>4</sub> NPs.

### Biosafety of Fe<sub>3</sub>O<sub>4</sub>-LA-PLGA NPs

The cytotoxicity of three different NPs (LA-PLGA NPs, Fe<sub>3</sub>O<sub>4</sub>-PLGA NPs, and Fe<sub>3</sub>O<sub>4</sub>-LA-PLGA NPs) was initially evaluated in MDA-MB-231 cells and a non-tumor cell line (HUVECs). The viability of MDA-MB-231 cells and HUVECs demonstrated a high cell survival rate even when various NPs were administered at the maximum concentration of 10 mg/mL without the application of ultrasound irradiation (Fig. 2A and B), indicating the favorable biocompatibility of the NPs. However, when exposed to ultrasound irradiation, the viability of MDA-MB-231 cells was significantly reduced, particularly when co-incubated with Fe<sub>3</sub>O<sub>4</sub>-LA-PLGA NPs (Fig. 2C), suggesting that ultrasound-triggered cytotoxicity due to the release of NO.

Moreover, a series of in vivo safety tests were conducted on the Fe<sub>3</sub>O<sub>4</sub>-LA-PLGA NPs, including blood cell analysis and biochemical examination. The blood biochemical parameters were not significantly different from the control group at any time point (Fig. 2D), thereby demonstrating the high biosafety of Fe<sub>3</sub>O<sub>4</sub>-LA-PLGA NPs. Furthermore, no significant damage was observed in major organs (heart, liver, spleen, lung, and kidney) based on H&E staining (Fig. 2E), indicating the excellent biocompatibility of the Fe<sub>3</sub>O<sub>4</sub>-LA-PLGA NPs.

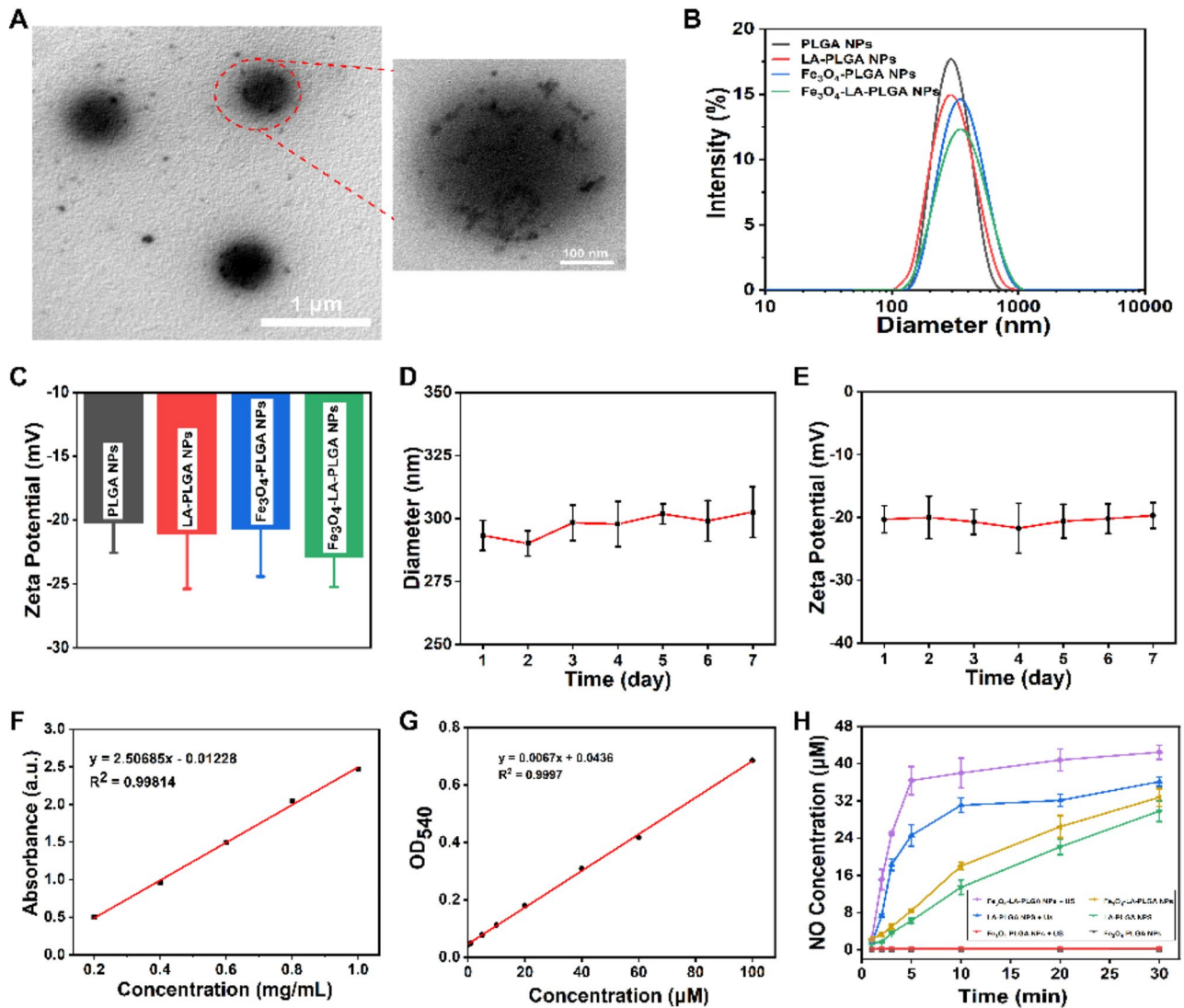


**Fig. 1** Characterization of  $\text{Fe}_3\text{O}_4$ -LA-PLGA NPs. **(A)** TEM images of  $\text{Fe}_3\text{O}_4$ -LA-PLGA NPs. **(B)** The hydrodynamic diameter and **(C)** Zeta potential of PLGA NPs, LA-PLGA NPs,  $\text{Fe}_3\text{O}_4$ -PLGA NPs, and  $\text{Fe}_3\text{O}_4$ -LA-PLGA NPs ( $n=3$ ). **(D)** The hydrodynamic diameter and **(E)** Zeta potential of  $\text{Fe}_3\text{O}_4$ -LA-PLGA NPs over an extended period of time ( $n=3$ ). **(F)** Standard curve of LA as a function of mass concentration via the UV-vis spectrometer. **(G)** Standard curve of NO via the Griess assay. **(H)** Release profiles of NO from various NPs with or without ultrasound irradiation, respectively ( $n=3$ )

**Ultrasound-responsive intracellular ROS and NO release**

As previously mentioned, the production of ROS plays a crucial role in oxidizing LA to generate a greater amount of NO. We employed the DCFH-DA probe to measure the intracellular ROS production in response to various NPs ( $\text{Fe}_3\text{O}_4$ -PLGA NPs, LA-PLGA NPs, and  $\text{Fe}_3\text{O}_4$ -LA-PLGA NPs). The results were depicted in Fig. S4, the most pronounced fluorescence intensity was detected in MDA-MB-231 cells that were treated with  $\text{Fe}_3\text{O}_4$ -LA-PLGA NPs in combination with ultrasound irradiation, followed by MDA-MB-231 cells treated with  $\text{Fe}_3\text{O}_4$ -PLGA NPs along with ultrasound irradiation. In contrast, merely minimal fluorescence signals were detected in the control, ultrasound-only, and LA-PLGA NPs only groups, indicating that the ultrasound-responsive

$\text{Fe}_3\text{O}_4$ -LA-PLGA NPs possess a remarkable capacity to generate a higher yield of ROS, which might have profound implications for LA oxidation and NO production.

A high concentration of NO is a critical factor in the efficacy of cancer therapy [42]. The intracellular NO release from  $\text{Fe}_3\text{O}_4$ -LA-PLGA NPs triggered by ultrasound was monitored using the NO-specific fluorescent probe (DAF-FM DA), which rapidly reacts with NO to produce benzotriazole and exhibits strong green fluorescence [43]. As shown in Fig. 3A, the most notable fluorescence was observed in MDA-MB-231 cells treated with  $\text{Fe}_3\text{O}_4$ -LA-PLGA NPs and ultrasound irradiation, followed by MDA-MB-231 cells treated with LA-PLGA NPs and ultrasound irradiation. In contrast, only a minimal fluorescence signal was detected in the control,

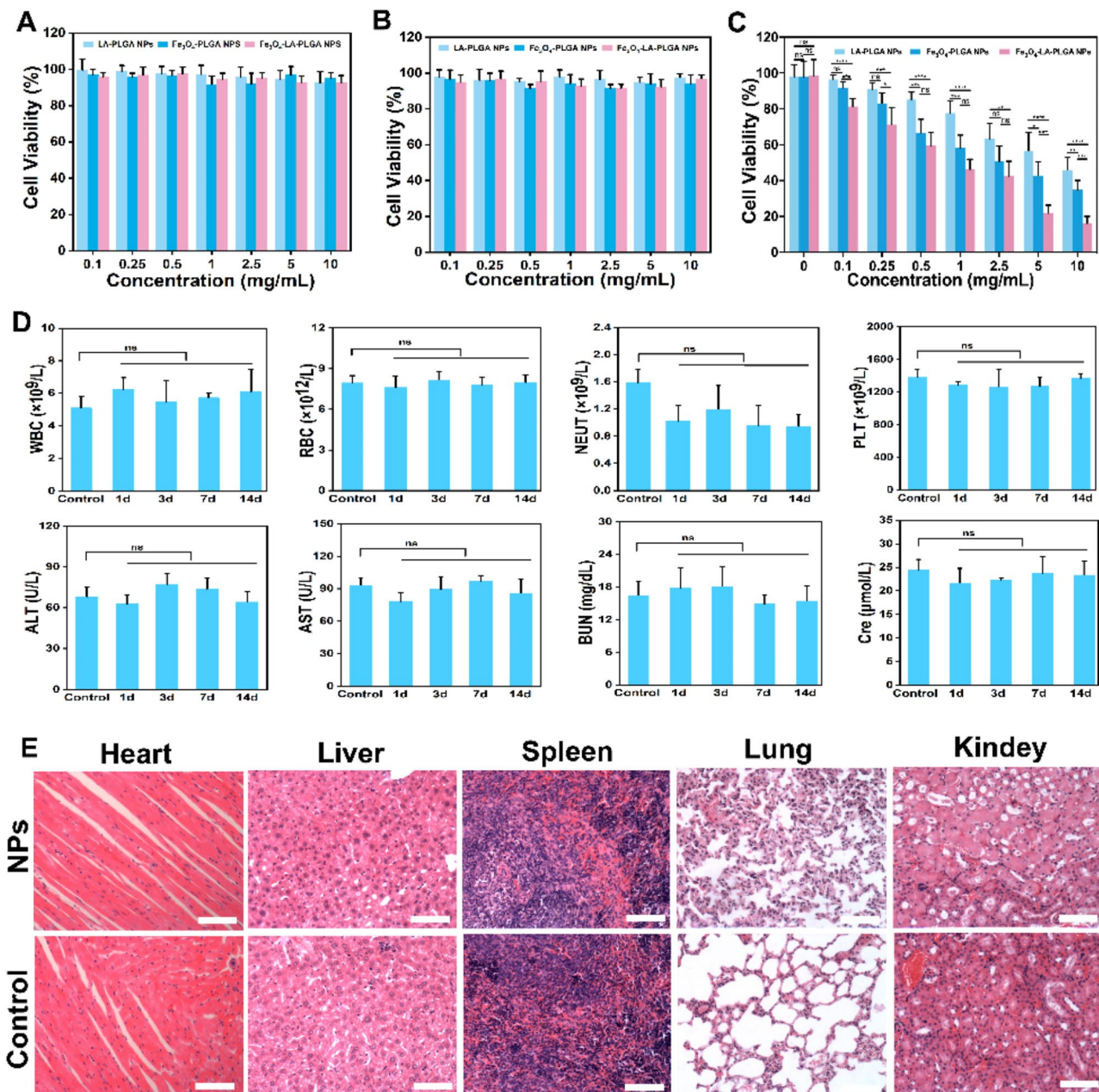


**Fig. 2** Biosafety evaluation of Fe<sub>3</sub>O<sub>4</sub>-LA-PLGA NPs. **(A)** The viability of MDA-MB-231 cells following incubation with distinct NPs (LA-PLGA NPs, Fe<sub>3</sub>O<sub>4</sub>-PLGA NPs, and Fe<sub>3</sub>O<sub>4</sub>-LA-PLGA NPs) for 24 h ( $n=5$ ). **(B)** The viability of HUVECs following incubation with different NPs (LA-PLGA NPs, Fe<sub>3</sub>O<sub>4</sub>-PLGA NPs, and Fe<sub>3</sub>O<sub>4</sub>-LA-PLGA NPs) for 24 h ( $n=5$ ). **(C)** The viability of MDA-MB-231 cells following incubation with different NPs (LA-PLGA NPs, Fe<sub>3</sub>O<sub>4</sub>-PLGA NPs, and Fe<sub>3</sub>O<sub>4</sub>-LA-PLGA NPs) for 4 h after ultrasound irradiation ( $n=5$ , \* $p<0.05$ , \*\* $p<0.01$ , \*\*\* $p<0.001$ , ns: not significant). **(D)** Hematological assay of BALB/c mice of the control group and the experimental groups at the corresponding time point ( $n=5$ , ns: not significant). **(E)** H&E staining of major organs (heart, liver, spleen, lung, and kidney) in the control group and the experimental groups at 14 days post-intravenous injection of Fe<sub>3</sub>O<sub>4</sub>-LA-PLGA NPs (Scale bar: 50 μm)

ultrasound-only, Fe<sub>3</sub>O<sub>4</sub>-PLGA NPs only, and Fe<sub>3</sub>O<sub>4</sub>-LA-PLGA NPs only groups, indicating the occurrence of ultrasound-responsive NO release. The quantitative analysis of average fluorescence intensity also showed the same results (Fig. 3B; \*\*\* $p<0.001$ ). Furthermore, calcein-AM and propidium iodide (PI) were utilized for co-staining viable and dead MDA-MB-231 cells to evaluate the NO-mediated cell viability. As anticipated, the majority

of the dead cells (red fluorescence) were observed in the group treated with Fe<sub>3</sub>O<sub>4</sub>-LA-PLGA NPs and ultrasound irradiation (Fig. 3C), indicating the highest percentage of dead MDA-MB-231 cells. The quantitative analysis of the percentage of red zones in the images also showed the same results (Fig. 3D; \*\*\* $p<0.001$ ). The aforementioned results confirm that the ultrasound-triggered NO release

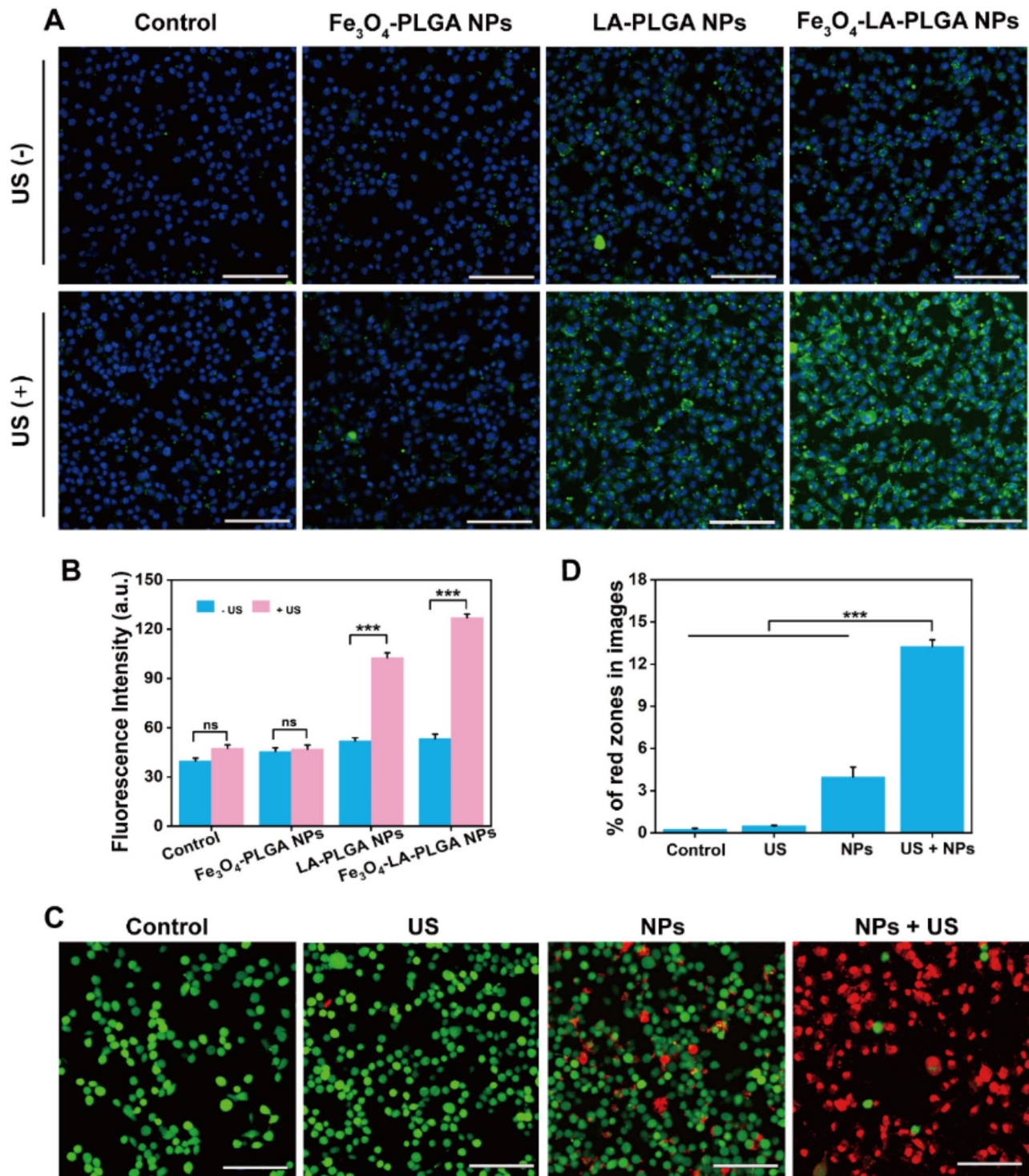


**Fig. 3** Intracellular NO release and in vitro cytotoxicity assay. **(A)** Representative CLSM images of DAF-FM DA-stained cells (Scale bar:100  $\mu$ m). **(B)** The average NO fluorescence intensity in tumor cells was quantified ( $n=3$ ,  $***p<0.001$ , ns: not significant). **(C)** MDA-MB-231 cells were stained with calcein-AM and PI following different treatments. (Scale bar: 100  $\mu$ m). **(D)** The percentage of red zones in the images was quantified ( $n=3$ ,  $***p<0.001$ )

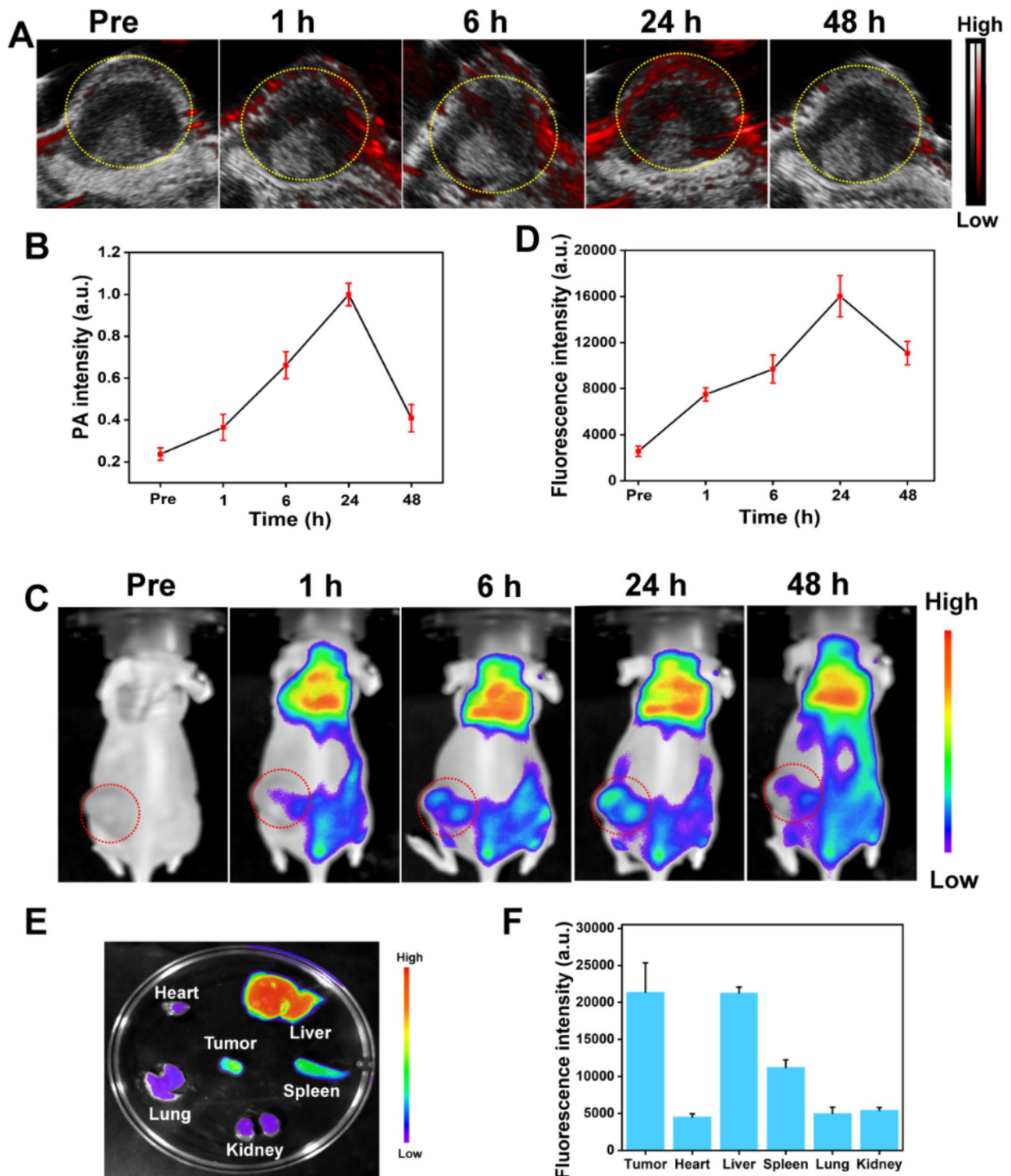


**Fig. 4** Dual-modality imaging of  $\text{Fe}_3\text{O}_4$ -LA-PLGA NPs. **(A)** PA images of tumors following intravenous injection of  $\text{Fe}_3\text{O}_4$ -LA-PLGA NPs at various time points (the yellow circle means the tumor location). **(B)** Quantitative analysis of PA intensity ( $n=3$ ). **(C)** In vivo FL imaging of tumor bearing mice at pre-injection, 1 h, 6 h, 24 h, and 48 h post-injection (the red circle means the tumor location). **(D)** Quantitative analysis of FL intensity ( $n=3$ ). **(E)** The biodistribution of DiR-labeled  $\text{Fe}_3\text{O}_4$ -LA-PLGA NPs in the tumor and major organs at 48 h post-injection is presented. **(F)** Quantitative analysis of FL intensity in tumor and major organs ( $n=3$ )

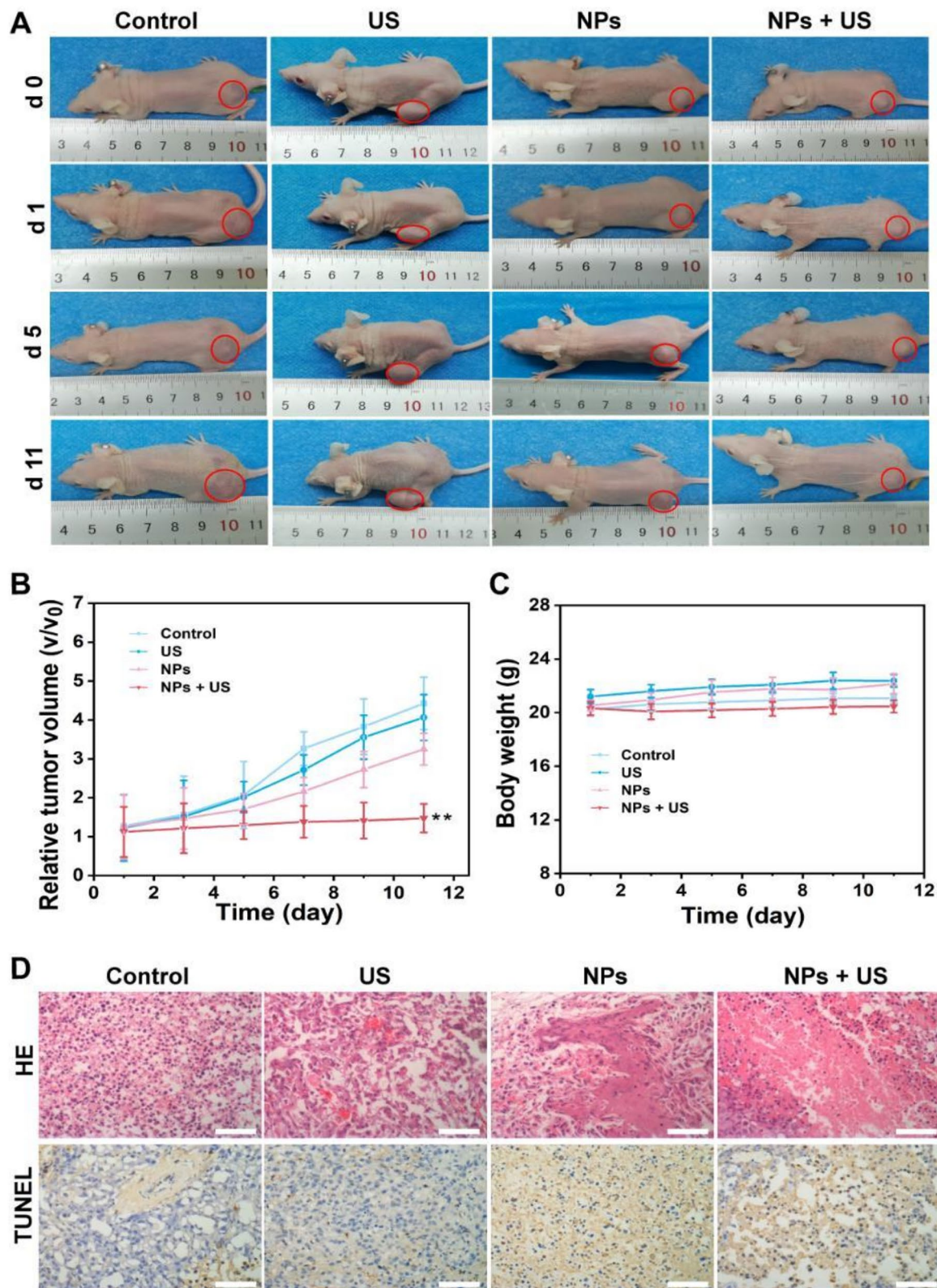


**Fig. 5** Evaluation of in vivo antitumor effects of Fe<sub>3</sub>O<sub>4</sub>-LA-PLGA NPs. **(A)** Digital images of tumor-bearing mice were obtained at the 11-day of different treatments. **(B)** Tumor growth trajectories of tumor-bearing mice post various treatments (*n* = 5). **(C)** Body weight measurements of tumor-bearing mice across different treatment groups (*n* = 5). **(D)** H&E staining and TUNEL staining of tumor sections from tumor-bearing mice subjected to various treatments (Scale bar: 50 μm)

from the reaction between  $\text{Fe}_3\text{O}_4$ -LA-PLGA NPs and  $\text{H}_2\text{O}_2$  present in the tumor is an effective process.

#### Dual-modality imaging of $\text{Fe}_3\text{O}_4$ -LA-PLGA NPs

The combination of PA imaging and FL imaging can compensate for the deficiencies of single imaging and provide comprehensive diagnosis and treatment information with high sensitivity and high resolution. As shown in Fig. 4A and B, the PA signals in the tumor region exhibited a gradual increase and reached a peak at 24 h post-intravenous injection of  $\text{Fe}_3\text{O}_4$ -LA-PLGA NPs, indicating the accumulation of  $\text{Fe}_3\text{O}_4$ -LA-PLGA NPs at the tumor site via the EPR effect. Additionally, FL imaging demonstrated the dynamic distribution of  $\text{Fe}_3\text{O}_4$ -LA-PLGA NPs in vivo, with a trend that aligned with that observed in PA imaging (Fig. 4C). The FL intensity also reached a peak 24 h after intravenous injection (Fig. 4D), indicating that the  $\text{Fe}_3\text{O}_4$ -LA-PLGA NPs were predominantly accumulated in the tumor region at this time point, which is crucial for subsequent in vivo treatment. Furthermore, the tumor tissues and excised organs were analyzed at 48 h post-injection to confirm the distribution of  $\text{Fe}_3\text{O}_4$ -LA-PLGA NPs. As shown by ex vivo imaging (Fig. 4E) and quantitative analysis (Fig. 4F), the highest FL intensity was observed in the liver, likely due to the phagocytosis by the reticuloendothelial system. These findings demonstrate that  $\text{Fe}_3\text{O}_4$ -LA-PLGA NPs exhibit dual-modality PA and FL imaging capabilities, facilitating precise diagnosis and effective treatment.

#### Therapeutic effects of $\text{Fe}_3\text{O}_4$ -LA-PLGA NPs

Encouraged by the evident ultrasound-responsive cytotoxicity of tumor cells, we undertook an evaluation of the in vivo antitumor efficacy of  $\text{Fe}_3\text{O}_4$ -LA-PLGA NPs through post-systemic administration. The MDA-MB-231 tumor-bearing nude mice were randomly divided into four groups and treated with the following interventions: (1) PBS as the control group, (2) ultrasound irradiation only (US), (3)  $\text{Fe}_3\text{O}_4$ -LA-PLGA NPs (containing 5 mg PLGA, with the same dose used for the subsequent groups, NPs), and (4)  $\text{Fe}_3\text{O}_4$ -LA-PLGA NPs+ultrasound irradiation (NPs+US). Tumor volumes and body weights were monitored throughout the experiment. Tumor volume was normalized with relative tumor volumes ( $V/V_0$ ). As shown in Fig. 5A and B, mice treated with PBS, “US”, and “NPs” exhibited a negligible therapeutic effect on tumor growth, while mice treated with “NPs+US” exhibited a significant inhibition of tumor growth compared to those of other groups (\*\* $p < 0.01$ ), suggesting that enhanced ultrasound-responsive NO release induced therapeutic effects. The mice’s body weights during the therapeutic period revealed minimal loss (Fig. 5C), indicating that  $\text{Fe}_3\text{O}_4$ -LA-PLGA NPs do not induce acute toxicity. Furthermore, histological

examination of tumor tissues via hematoxylin and eosin (H&E) staining and terminal deoxynucleotidyl transferase dUTP nick end labeling (TUNEL) assay demonstrated the efficacy of NO-induced therapeutic effects (Fig. 5D). As shown by H&E staining of tumor tissues, mice treated with “NPs+US” exhibited numerous deformed nuclei (karyopyknosis, karyorrhexis, and karyolysis), indicative of severe tumor cell necrosis. Furthermore, the TUNEL assay revealed a greater number of apoptotic cells in the tumor tissues of the treated group compared to the other control groups.

#### Conclusions

In conclusion, the ultrasound-responsive nanoplatform, consisting of PLGA,  $\text{Fe}_3\text{O}_4$ , and LA was successfully constructed for the rapid and controlled release of NO, which inhibits the growth of breast cancer. Compared with other traditional stimulus-responsive NO-delivery nanoplatforms, our resultant nanoplatform demonstrated several advantages, including: (i) an ultrasound-responsive strategy for PLGA NPs loaded with LA and  $\text{Fe}_3\text{O}_4$  NPs; (ii) a cascade amplification reaction for a rapid and large amount of NO production; and (iii) real-time imaging monitoring via PA and FL dual-modality imaging; and (iv) effective therapeutic effects by NO-assisted antitumor gas therapy.

#### Supplementary Information

The online version contains supplementary material available at <https://doi.org/10.1186/s12935-024-03627-4>.

Supplementary Material 1

#### Acknowledgements

Not applicable.

#### Author contributions

Haiyan Yang: Conceptualization, Writing—original draft. Guangrong Zheng: Methodology, Investigation. Guochen Li: Visualization, Software. Jincui Chen, Yong Luo: Methodology, Project administration. Licui Qi: Data curation. Tengfei Ke: Formal analysis, Data curation. Jie Xiong: Writing – review & editing. Xiaojuan Ji: Project administration. All authors reviewed the manuscript.

#### Funding

This work was supported by the Natural Science Foundation of Chongqing (CSTB2024NSCQ-MSX0102), Chongqing Medical Youth Top-notch Talent (YXQN202446), Chongqing Postdoctoral Science Foundation (2023CQBSHTB1005 and CSTB2023NSCQ-BHX0035), Chongqing women and Children General Project Fund (2020FY108), and Graduate Innovation Foundation of Kunming Medical University (2024S122 and 2024B013).

#### Data availability

No datasets were generated or analysed during the current study.

#### Declarations

#### Ethical approval

The authors are accountable for all aspects of the work in ensuring that questions related to the accuracy or integrity of any part of the work are appropriately investigated and resolved. The animal study protocol was

approved by the Ethics Committee of Chongqing Medical University (IACUC-CQMU-2023-10060).

### Competing interests

The authors declare no competing interests.

Received: 1 October 2024 / Accepted: 20 December 2024

Published online: 28 December 2024

### References

- Chatterji S, Krzoska E, Thoroughgood CW, Saganty J, Liu P, Elsberger B, Abu-Eid R, Speirs V. Defining genomic, transcriptomic, proteomic, epigenetic, and phenotypic biomarkers with prognostic capability in male breast cancer: a systematic review. *Lancet Oncol*. 2023;24(2):e74–85.
- Tsai CJ, Yang JT, Shaverdian N, Patel J, Shepherd AF, Eng J, Guttman D, Yeh R, Gelblum DY, Namakhdoust A, et al. Standard-of-care systemic therapy with or without stereotactic body radiotherapy in patients with oligoprogressive breast cancer or non-small-cell lung cancer (consolidative use of Radiotherapy to Block [CURB] oligoprogression): an open-label, randomised, controlled, phase 2 study. *Lancet*. 2024;403(10422):171–82.
- Gradishar WJ, Moran MS, Abraham J, Abramson V, Aft R, Agnese D, Allison KH, Anderson B, Burstein HJ, Chew H, et al. NCCN Guidelines® insights: breast Cancer, Version 4.2023. *J Natl Compr Canc Netw*. 2023;21(6):594–608.
- Kunkler IH, Williams LJ, Jack WJL, Cameron DA, Dixon JM. Breast-conserving surgery with or without irradiation in early breast Cancer. *N Engl J Med*. 2023;388(7):585–94.
- Bartels SAL, Donker M, Poncet C, Sauv e N, Straver ME, van de Velde CJH, Mansel RE, Blanken C, Orzalesi L, Klinkenbijl JHG, et al. Radiotherapy or surgery of the Axilla after a positive sentinel node in breast Cancer: 10-Year results of the Randomized Controlled EORTC 10981–22023 AMAROS trial. *J Clin Oncol*. 2023;41(12):2159–65.
- Kuerer HM, Smith BD, Krishnamurthy S, Yang WT, Valero V, Shen Y, Lin H, Lucci A, Boughey JC, White RL, et al. Eliminating breast surgery for invasive breast cancer in exceptional responders to neoadjuvant systemic therapy: a multicentre, single-arm, phase 2 trial. *Lancet Oncol*. 2022;23(12):1517–24.
- Asleh K, Negri GL, Spencer Miko SE, Colborne S, Hughes CS, Wang XQ, Gao D, Gilks CB, Chia SKL, Nielsen TO, et al. Proteomic analysis of archival breast cancer clinical specimens identifies biological subtypes with distinct survival outcomes. *Nat Commun*. 2022;13(1):896.
- Pedersen RN, Esen B, Mellemkj er L, Christiansen P, Ejlersen B, Lash TL, N rsgaard M, Cronin-Fenton D. The incidence of breast Cancer recurrence 10–32 years after primary diagnosis. *J Natl Cancer Inst*. 2022;114(3):391–9.
- Nattinger AB, Bickell NA, Schymura MJ, Laud P, McGinley EL, Fergstrom N, Pezzin LE. Centralization of Initial Care and improved survival of poor patients with breast Cancer. *J Clin Oncol*. 2023;41(11):2067–75.
- Wan SS, Zeng JY, Cheng H, Zhang XZ. ROS-induced NO generation for gas therapy and sensitizing photodynamic therapy of tumor. *Biomaterials*. 2018;185:51–62.
- Wang K, Li Y, Wang X, Zhang Z, Cao L, Fan X, Wan B, Liu F, Zhang X, He Z, et al. Gas therapy potentiates aggregation-induced emission luminogen-based photoimmunotherapy of poorly immunogenic tumors through cGAS-STING pathway activation. *Nat Commun*. 2023;14(1):2950.
- Wang Y, Qian M, Du Y, Zhou J, Huo T, Guo W, Akhtar M, Huang R. Tumor-selective biodegradation-regulated photothermal H(2) S donor for Redox Dyshomeostasis- and glycolysis disorder-enhanced theranostics. *Small*. 2022;18(8):e2106168.
- Zhu D, Liu Z, Li Y, Huang Q, Xia L, Li K. Delivery of manganese carbonyl to the tumor microenvironment using tumor-derived exosomes for cancer gas therapy and low dose radiotherapy. *Biomaterials* 2021, 274:120894.
- Rankine LJ, Wang Z, Kelsey CR, Bier E, Driehuis B, Marks LB, Das SK. Hyperpolarized (129)xe magnetic resonance imaging for functional avoidance treatment planning in thoracic Radiation Therapy: a comparison of ventilation- and gas exchange-guided treatment plans. *Int J Radiat Oncol Biol Phys*. 2021;111(4):1044–57.
- Gao H, Cao Z, Liu H, Chen L, Bai Y, Wu Q, Yu X, Wei W, Wang M. Multifunctional nanomedicines-enabled chemodynamic-synergized multimodal tumor therapy via Fenton and Fenton-like reactions. *Theranostics*. 2023;13(6):1974–2014.
- He T, Qin X, Jiang C, Jiang D, Lei S, Lin J, Zhu WG, Qu J, Huang P. Tumor pH-responsive metastable-phase manganese sulfide nanotheranostics for traceable hydrogen sulfide gas therapy primed chemodynamic therapy. *Theranostics*. 2020;10(6):2453–62.
- Zhang Z, Zhang L, Huang C, Guo Q, Zuo Y, Wang N, Jin X, Zhang L, Zhu D. Gas-generating mesoporous silica nanoparticles with rapid localized drug release for enhanced chemophotothermal tumor therapy. *Biomater Sci*. 2020;8(23):6754–63.
- Cheng J, Zhu Y, Dai Y, Li L, Zhang M, Jin D, Liu M, Yu J, Yu W, Su D, et al. Gas-mediated Tumor Energy Remodeling for sensitizing mild Photothermal Therapy. *Angew Chem Int Ed Engl*. 2023;62(27):e202304312.
- Ji C, Zheng X, Li S, Liu C, Yin M. Perylenediimides with enhanced autophagy inhibition for a dual-light activatable Photothermal Gas Therapy. *ACS Appl Mater Interfaces*. 2023;15(29):34427–35.
- Zhang M, Liu X, Mao Y, He Y, Xu J, Zheng F, Tan W, Rong S, Chen Y, Jia X, et al. Oxygen-Generating hydrogels overcome Tumor Hypoxia to enhance Photodynamic/Gas synergistic therapy. *ACS Appl Mater Interfaces*. 2022;14(24):27551–63.
- Zhang Y, Zhang X, Yang H, Yu L, Xu Y, Sharma A, Yin P, Li X, Kim JS, Sun Y. Advanced biotechnology-assisted precise sonodynamic therapy. *Chem Soc Rev*. 2021;50(20):11227–48.
- Fan W, Yung BC, Chen X. Stimuli-Responsive NO. Release for On-Demand gas-sensitized synergistic Cancer therapy. *Angew Chem Int Ed Engl*. 2018;57(28):8383–94.
- Huang X, Xu F, Hou H, Hou J, Wang Y, Zhou S. Stimuli-responsive nitric oxide generator for light-triggered synergistic cancer photothermal/gas therapy. *Nano Res*. 2019;12(6):1361–70.
- Andrabi SM, Sharma NS, Karan A, Shahriar SMS, Cordon B, Ma B, Xie J. Nitric oxide: physiological functions, delivery, and Biomedical Applications. *Adv Sci (Weinh)*. 2023;10(30):e2303259.
- Jiang Z, Zhang C, Sun Q, Wang X, Chen Y, He W, Guo Z, Liu Z. A NIR-II photoacoustic probe for high spatial quantitative imaging of Tumor nitric oxide in vivo. *Angew Chem Int Ed Engl*. 2024;63(19):e202320072.
- Liu X, Wang M, Jiang Y, Zhang X, Shi C, Zeng F, Qin Y, Ye J, Hu J, Zhou Z. Magnetic resonance imaging nanoprobe quantifies nitric oxide for evaluating M1/M2 macrophage polarization and prognosis of Cancer treatments. *ACS Nano*. 2023;17(24):24854–66.
- Liu W, Semcheddine F, Guo Z, Jiang H, Wang X. Near-Infrared light-triggered nitric oxide nanogenerators for NO-Photothermal synergistic Cancer therapy. *Nanomaterials (Basel)*. 2022;12(8):1348.
- Jin Z, Wen Y, Hu Y, Chen W, Zheng X, Guo W, Wang T, Qian Z, Su BL, He Q. MRI-guided and ultrasound-triggered release of NO by advanced nanomedicine. *Nanoscale*. 2017;9(10):3637–45.
- Fan J, He N, He Q, Liu Y, Ma Y, Fu X, Liu Y, Huang P, Chen X. A novel self-assembled sandwich nanomedicine for NIR-responsive release of NO. *Nanoscale*. 2015;7(47):20055–62.
- Liu P, Wang Y, Liu Y, Tan F, Li J, Li N. S-nitrosothiols loaded mini-sized Au@silica nanorod elicits collagen depletion and mitochondrial damage in solid tumor treatment. *Theranostics*. 2020;10(15):6774–89.
- Arora H, Panara K, Kuchakulla M, Kulandavelu S, Burnstein KL, Schally AV, Hare JM, Ramasamy R. Alterations of tumor microenvironment by nitric oxide impedes castration-resistant prostate cancer growth. *Proc Natl Acad Sci USA*. 2018;115(44):11298–303.
- Mena-Osuna R, Mantrana A, Guil-Luna S, S nchez-Montero MT, Navarrete-Sirvent C, Morales-Ruiz T, Rivas-Crespo A, Toledano-Fonseca M, Garc a-Ortiz MV, Garc a-Jurado G, et al. Metabolic shift underlies tumor progression and immune evasion in S-nitrosoglutathione reductase-deficient cancer. *J Pathol*. 2023;260(3):261–75.
- Kudo S, Nagasaki Y. A novel nitric oxide-based anticancer therapeutics by macrophage-targeted poly(l-arginine)-based nanoparticles. *J Control Release*. 2015;217:256–62.
- Jiang L, Wang K, Qiu L. Doxorubicin hydrochloride and L-arginine co-loaded nanovesicle for drug resistance reversal stimulated by near-infrared light. *Asian J Pharm Sci*. 2022;17(6):924–37.
- Chen Q, Feng L, Liu J, Zhu W, Dong Z, Wu Y, Liu Z. Intelligent Albumin–MnO<sub>2</sub> nanoparticles as pH-/H<sub>2</sub>O<sub>2</sub>-Responsive Dissociable nanocarriers to modulate Tumor Hypoxia for Effective Combination Therapy. *Adv Mater*. 2016;28(33):7129–36.
- Yang H, Jiang F, Zhang L, Wang L, Luo Y, Li N, Guo Y, Wang Q, Zou J. Multifunctional l-arginine-based magnetic nanoparticles for multiple-synergistic tumor therapy. *Biomater Sci*. 2021;9(6):2230–43.
- Huo M, Wang L, Chen Y, Shi J. Tumor-selective catalytic nanomedicine by nanocatalyst delivery. *Nat Commun*. 2017;8(1):357.

38. Li WP, Su CH, Chang YC, Lin YJ, Yeh CS. Ultrasound-Induced reactive oxygen species mediated Therapy and Imaging using a Fenton reaction Activable Polymersome. *ACS Nano*. 2016;10(2):2017–27.
39. Zhang K, Xu H, Jia X, Chen Y, Ma M, Sun L, Chen H. Ultrasound-triggered nitric oxide release platform based on Energy Transformation for targeted inhibition of pancreatic tumor. *ACS Nano*. 2016;10(12):10816–28.
40. Ewii UE, Onugwu AL, Nwokpor VC, Akpaso I-a, Ogbulie TE, Aharanwa B, Chijioke C, Verla N, Iheme C, Ujowundu C, Anyiam C, Attama AA. Novel drug delivery systems: insight into self-powered and nano-enabled drug delivery systems. *Nano TransMed*. 2024;3:100042.
41. Yang D, Chen Q, Zhang M, Feng G, Sun D, Lin L, Jing X. Drug-loaded acoustic nanodroplet for dual-imaging guided highly efficient chemotherapy against nasopharyngeal carcinoma. *Int J Nanomed*. 2022;17:4879–94.
42. Confino H, Sela Y, Epshtein Y, Malka L, Goldshtein M, Chaisson S, Lisi S, Avniel A, Monson JM, Dirbas FM. Intratumoral Administration of High-Concentration Nitric Oxide and Anti-mPD-1 treatment improves Tumor Regression Rates and Survival in CT26 Tumor-Bearing mice. *Cells*. 2023, 12(20).
43. Liu S, Sun Y, Zhang T, Cao L, Zhong Z, Cheng H, Wang Q, Qiu Z, Zhou W, Wang X. Upconversion nanoparticles regulated drug & gas dual-effective nanoplat-form for the targeting cooperated therapy of thrombus and anticoagulation. *Bioac Mater*. 2022;18:91–103.

### Publisher's note

Springer Nature remains neutral with regard to jurisdictional claims in published maps and institutional affiliations.